Article

The Influence of the Process Conditions on the Thermo-Mechanical Fatigue Damage of the Rolls in the Twin-Roll Casting Process of Aluminum Alloys

Ratibor Shevchenko *[ID], Nicola Zani [ID] and Angelo Mazzù [ID]

Department of Mechanical and Industrial Engineering, University of Brescia, Via Branze 38, 25123 Brescia, Italy; nicola.zani@unibs.it (N.Z.); angelo.mazzu@unibs.it (A.M.)
* Correspondence: r.shevchenko@unibs.it

Abstract: Twin-roll casting is a technology for the production of thin strips directly from liquid metal by combining continuous casting with hot rolling in a single step. The thermo-mechanical cyclic interaction with the solidifying strip causes fatigue crack formation at the outer surface of the rolls. A 2D FEM model with Eulerian boundary conditions and the interference fit load on the rolls was defined. The influence of the roll–strip thermal contact, the inlet temperature of the liquid aluminum, the efficiency of the water cooling and the production rate on the fatigue damage of the rolls was analyzed with a parametric study. The maximum temperature of the rolls, the maximum contact pressure, the accumulated plastic strain and the equivalent strain computed (considering a multiaxial out-of-phase fatigue criterion) were considered to investigate the thermo-mechanical fatigue load on the rolls. The results showed that, in the considered range, the most influential parameters on the fatigue mechanism are the heat contact conductance coefficient, which dominates the thermo-mechanical load, and the tangential velocity of the rolls, which contributes to the thermal field and determines the roll–strip mechanical contact interaction.

Keywords: twin-roll casting; thermo-mechanical stresses; multiaxial fatigue; finite elements

1. Introduction

Twin-roll casting is a technology for the production of thin strips about 1 mm to 10 mm thick. The process was devised by Henry Bessemer [1] and involves the production of the strips directly from liquid metal by combining continuous casting with hot rolling in a single step. The operating principle is based on the rapid solidification of the liquid metal on internally cooled rotating rolls and on the mechanical action of these rolls on the strip [2,3]. Compared to the more traditional processes [4], twin-roll casting allows a reduction in production steps, energy savings and lower investment costs [5], while also allowing for recycled materials [6]. The microstructure and mechanical properties of the finished product are also considerable [7–9] and are still the object of research [10–13].

There are three main types of twin-roll casting according to the direction of the molten metal flow: horizontal, with the axes of the rolls arranged vertically one above the other [14]; vertical, with the axes on the horizontal plane [15]; and an inclined configuration [7].

The operating conditions of the rolls depend on thermal factors, fluid dynamics and mechanical interactions between the rolls and the strip [16]. The main parameters that influence these aspects are the superheat temperature of the melted metal, the configuration of the nozzle, the presence or absence of lubricant between the rolls and the strip, the thickness of the strip, the rotation speed of the rolls, heat and force exchanged (roll separation force) between the rolls and the strip [17], the rolls' material (steel or copper) and their diameter.

There have been several studies that carry out a thermo-fluid dynamic analysis of the process, often performed by a numerical method with 2D or 3D models [18]. The models

have investigated the solidification of the metal, distinguishing the liquid, solid and an intermediate liquid–solid zone (mushy zone) and identifying turbulent flows in the molten area [19]. The amplitude of the mushy zone influences the mechanical force exchanged between the rolls and the strip and the properties of the product [20]. The proposed models take into account possible turbulence, solidification, thermal fluxes to the environment and the heat exchange between the rolls and the strip, identifying the heat transfer coefficient as one of the most important parameters [21]. From a fluid dynamics point of view, the liquid–solid strip can be represented as a mono-phase or bi-phase material, modeling the semi-solid area (mushy zone) like a substance with variable viscosity [22–24].

Studies relating specifically to the analysis of stresses and strains in the twin-roll casting process, on the other hand, seem to be few and not easily available, and they mainly concern the strip produced [12].

The wear of the rolls in the twin-roll casting process of steel was experimentally studied by Zapuskalov et al. [25], investigating the surface roughness of the roll and showing the influence of the erosive action due to the flow of processed material on the component.

Stress analysis in both the strip and rolls was studied by Saxena et al. [26]. Stresses due to friction between the rolls and the strip were not considered, and the roll separating force was calculated analytically and then applied on the components. The liquid–solid metal was modeled as a viscoplastic material by adjusting the Poisson coefficient and the Young modulus to treat the liquid. The analysis showed the arising of high compression stresses on the surface of the roll due to thermal load and compression force on the rolls, identifying the conditions for the onset of fatigue.

Hadadzadeh et al. [20] developed a 2D model of the top-half part of the group roll/strip. The solidification process and the zone of liquid–solid transition (mushy zone) were taken into consideration. The rolls were assumed to be rigid and the interaction between the roll and the strip was modeled considering the friction according to Coulomb's law.

The influence on the interaction force between the strip and the rolls, the asymmetrical rotation speed of the rolls and the configuration of the nozzle has been studied by Lee et al. [16]. The values obtained from the numerical simulation were compared with the force values measured experimentally, showing the convergence of the respective values over time.

The twin-roll casting process has received a growing interest in recent decades. The parameters of the process and their influence on the product have been studied, but not much has been carried out to specifically analyze the conditions of the rolls. The objective of this work is to study the thermo-mechanical state and the damage conditions in relation to the rolls' life expectancy in the twin-roll casting process of aluminum alloys.

Rolls are an important component, not only for their cost, but also for the required reliability necessary to ensure the continuous productivity of the process.

Due to the thermo-mechanical conditions at the outer surface of the roll, wear damage occurs and cracks form [27]. These cracks can generate defects and determine the production of a low-quality strip. The propagation of the cracks can cause the failure of the roll [28]. To avoid the failure of the rolls and to ensure a good-quality product, it is important to perform roll maintenance operations. Hence, it is necessary to investigate the damaging phenomena at the outer surface of the rolls by considering different operating conditions.

This is possible by developing a thermo-mechanical numerical model of the rolls to predict their stress and strain state during the process. In order to investigate the damage phenomena and to predict the crack initiation, the influence of the main process parameters is considered. A proper fatigue index is considered to compare the expected damage in different process conditions.

2. Materials and Methods

A 2D schematic of the horizontal twin-roll thin-strip caster with all dimensions is illustrated in Figure 1. The geometrical data taken into account are shown in Table 1.
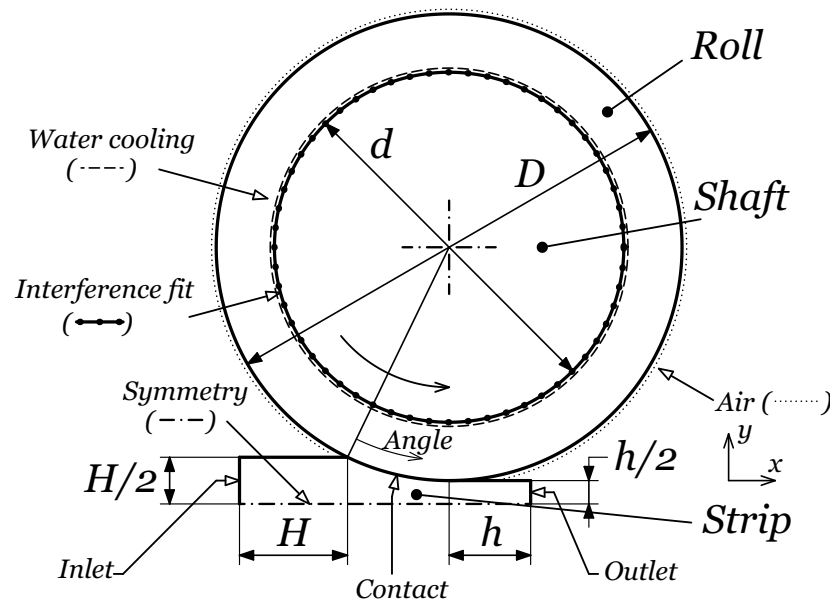

Figure 1. Schematic representation of the twin-roll casting process with relevant modeling parameters.

Table 1. Geometrical data of the roll and the strip.

Symbol	Description	Value
D	Outer diameter of the rolls	660 mm
d_{roll}	Inner diameter of the rolls	545 mm
d_{shaft}	Diameter of the shaft	545.55 mm
H	Inlet nozzle height	14 mm
h	Outlet strip height	8 mm

An explicit thermo-mechanical 2D plane-strain FEM was defined by using Abaqus 2020 FEA software. The symmetry of the problem was considered and the top-half part of the strip–roll–shaft geometry was modeled. Lagrangian analysis was used, but the Eulerian boundary conditions [29] at the inlet and the outlet zones were imposed. This allowed us to model a limited portion of the strip during the whole simulation and to avoid unwanted mesh deformations. To reach the steady-state conditions during the process while considering the time cost of the numerical simulation, 8 rotations of the rolls were performed. The attainment of the steady-state conditions was verified a posteriori by considering the thermo-mechanical state history of the rolls during the simulations.

The reference conditions for the simulation were considered as follows: $T_{superheat} = 40\,°C$, $u_{roll} = 16\,\frac{mm}{s}$, $h_{water} = 10\,\frac{kW}{m^2°C}$ and $h_{contact} = 15\,\frac{kW}{m^2°C}$. Then, a parametric study was performed by varying 4 process parameters through 5 levels:

1. Strip–roll contact conductance coefficient, $h_{contact}$, which represents the thermal efficiency of the heat-removing process from the strip during the production;
2. The liquid aluminum superheat, $T_{superheat}$, related to the initial temperature of the liquid aluminum poured though the nozzle between the rolls;
3. Water-cooling heat transfer coefficient, h_{water}, related to the intensity and efficacy of the cooling system at the internal surface of the rolls;
4. The tangential velocity of the rolls, u_{roll}, representing (and proportional to) the production rate of the finite product.

To analyze the impact of the process conditions on the thermo-mechanical load and fatigue, 4 indicators were considered:

1. Maximum temperature, T_{max}, reached by the roll during the rotation;
2. Maximum contact pressure, $|\sigma_r|_{max}$, which represents the mechanical load due to the strip–roll contact interaction;
3. Accumulated plastic strain, ε_{pl}, at the external surface of the roll after 8 rotations;
4. Equivalent strain value, ε_{eq}, which is related through the life curve to the number of cycles required to cause the crack initiation.

2.1. Material Modeling

The data to model the thermal and mechanical behavior of the material of the roll and the mechanical properties of the material of the strip presented below were provided by the manufacturer of the rolls.

2.1.1. Rolls

The material of the rolls was modeled as an elastic–plastic solid. The Von Mises yield surface and the associative flow rule were considered. A temperature-dependent non-linear kinematic hardening behavior was implemented according the Armstrong–Frederick law [30]. The plastic behavior of the rolls was modeled considering the experimental hardening curves represented in Figure 2.

The temperature-non-dependent parameters are density $\rho = 7830 \, \text{kg/m}^3$, specific heat $c_p = 502 \, \text{J/kg}°\text{C}$ and Poisson's ration $\nu = 0.3$. The temperature-dependent properties are indicated in Table 2. The reference temperature for the considered thermal expansion is $T_{ref} = 25 \, °\text{C}$.
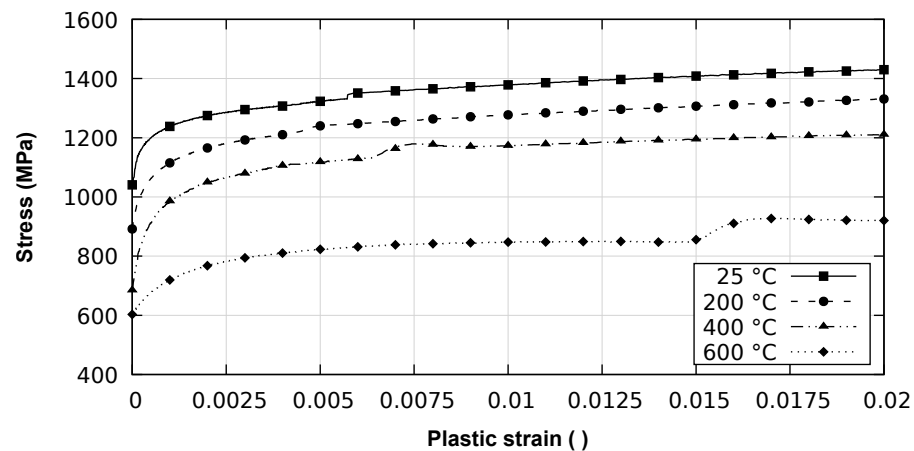

Figure 2. Hardening curve data of the rolls.

Table 2. Temperature-dependent material properties of the rolls.

T (°C)	E (MPa)	α ($\times 10^{-5}$)	k (W/m°C)
25	210,000	1.238	30.3
100	200,000	1.238	30.48
200	197,000	1.303	30.9
300	188,000	1.362	31.56
400	194,000	1.406	31.2
500	185,000	1.435	32
600	140,000	1.465	32.8
660	124,000	1.465	32.8

2.1.2. Strip

The aluminum strip was treated as an elastic–plastic material with linear isotropic hardening. The thermo-physical data (density, thermal conductivity, specific heat) were implemented according to the A1-6061-T6 alloy, referring to [31]. The latent heat during the solidification of the aluminum was also taken into account. The dependence of the Young modulus of the strip E_{strip}, plastic hardening modulus of the strip E_{pl} (the slope of the stress versus plastic strain curve) and the yield stress of the strip σ_y with respect to the temperature are shown in Figure 3. The Poisson's ration of the strip was considered as $\nu_{strip} = 0.33$. Table 3 indicates the thermal expansion values α_{strip} for different temperatures of the material of the strip with reference temperature $T_{ref} = 25\,^\circ$C.

Table 3. Thermal expansion α_{strip} of the material of the strip.

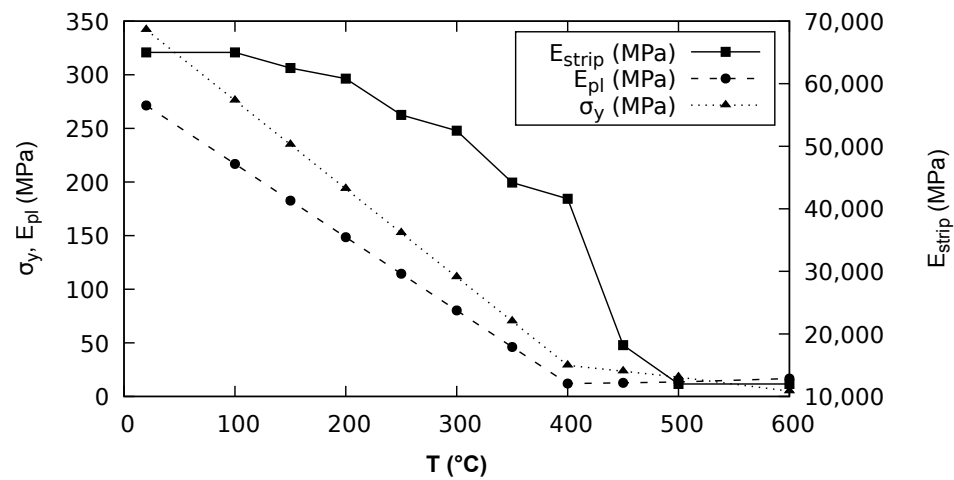| T (°C)	α_{strip} $(\times 10^{-5})$
20	2.245
100	2.287
200	2.656
300	2.746
400	2.910
500	3.192
600	3.513

Figure 3. Elastic–plastic properties of the material of the strip.

2.1.3. Shaft

The shaft was modeled as an elastic solid with the Young modulus $E_{shaft} = 210,000\,$MPa and Poisson's ratio $\nu_{shaft} = 0.3$.

2.2. Boundary Conditions and Interactions

Reference process conditions and parameter variations were defined, with reference to the studies present in the literature, relative to the aluminum alloy strip production [19,21,23,32]. The levels of varied parameters were defined according to the cited studies in order to investigate a reasonably wide range of physical conditions [33].

2.2.1. Initial Conditions

- The initial temperature of the roll and the shaft were considered as equal to the environmental temperature $T_{0_{roll}} = T_{0_{shaft}} = T_0 = 25\,^\circ$C;

- The initial temperature of the strip was equal to the inlet temperature $T_{0_{strip}} = T_{inlet} = T_{liquidus} + T_{superheat}$ and varied according to the $T_{superheat}$ parameter. The reference values considered were $T_{superheat} = 40\ ^\circ$C and $T_{0_{strip}} = 682\ ^\circ$C.

2.2.2. Mechanical Conditions

- The symmetry condition at the middle axes of the strip was defined.
- The shaft rotation speed was imposed according to the tangential velocity u_{roll} of the rolls to achieve. The reference value for the tangential velocity was $u_{roll} = 16$ mm/s. Five levels were investigated, as indicated in Table 4;
- The interference fit interaction between the roll (inner surface in Figure 1) and the shaft was computed by considering the rough friction model according to the geometry and thermal conditions of the parts during the whole simulation;
- The nodes of the inlet surface were fixed considering the coordinate system for the strip in Figure 1 ($u_x = u_y = 0$ mm). The nodes of the outlet surface were constrained to remain on the same plane, avoiding the longitudinal displacements ($u_x = 0$ mm).

Table 4. Physical data and casting conditions of the process.

Symbol	Description	Value
H_f	Heat of fusion of aluminum	336,000 J/kg
$T_{liquidus}$	Liquidus temperature	642 °C
$T_{solidus}$	Solidus temperature	600 °C
h_{air}	Rolls–air heat transfer coefficient	0.02 kW/m^2 °C
T_0	Environment temperature	25 °C
$T_{superheat}$	Liquid aluminum superheat	20–30–40–50–60 (°C)
T_{inlet}	Melt inlet temperature	$T_{inlet} = T_{liquidus} + T_{superheat}$
u_{roll}	Tangential velocity of the rolls	4–8–16–24–32 (mm/s)
h_{water}	Water-cooling heat transfer coefficient	1–5–10–15–20 (kW/m^2 °C)
T_{water}	Water-cooling reference temperature	25 °C
$h_{contact}$	Strip–roll contact conductance coefficient	5–10–15–20–25 (kW/m^2 °C)

2.2.3. Thermal Conditions

- The inlet temperature of the liquid metal at the inlet nozzle was the constraint $T_{inlet} = T_{liquidus} + T_{superheat} = 682\ ^\circ$C;
- The heat fluxes due to water-cooling system were computed as follows:

$$q_{water} = h_{water}\left(T_{roll} - T_{water}\right) \tag{1}$$

where q_{water} is the specific heat flux at a point on the inner surface of the roll, T_{roll} is the temperature of the point and $T_{water} = 25\ ^\circ$C is the water-cooling reference temperature. The water-cooling heat transfer coefficient h_{water} varies according to Table 4 with the reference value $h_{water} = 10$ kW/m^2 °C;

- The heat fluxes between the outer surface of the roll and the surrounding air were computed as follows:

$$q_{air} = h_{air}\left(T_{roll} - T_{air}\right) \tag{2}$$

where the reference temperature of the air $T_{air} = T_0 = 25\ ^\circ$C and the heat transfer coefficient $h_{air} = 0.02$ kW/m^2 °C.

2.2.4. Roll–Strip Contact

The roll–strip mechanical contact was defined by assuming the Coulomb friction model with the friction coefficient $f = 0.61$. The thermal contact was defined by considering a contact conductance coefficient relative to the following heat flux equation:

$$q_{roll-strip} = h_{contact}\left(T_{roll} - T_{strip}\right) \tag{3}$$

where $q_{roll-strip}$ is the specific heat flux between points in contact and T_{roll} and T_{strip} are, respectively, the temperature of the roll and strip points in contact. The contact conductance coefficient $h_{contact}$ was varied through five values, as shown in Table 4, and its reference value was $h_{contact} = 15 \, \text{kW/m}^2 \, ^\circ\text{C}$.

2.3. Numerical Settings

To perform the simulation the plane strain mesh was defined with the characteristics presented in Table 5. The adaptive mesh was used for the strip in order to define Eulerian boundary conditions. The global and local view of the mesh are represented in Figure 4. In order to reach a reasonable time of execution, a mass-scaling technique was adopted. The value for target time increment for the explicit iteration was calibrated a posteriori to minimize the influence of the mass scaling on the results.
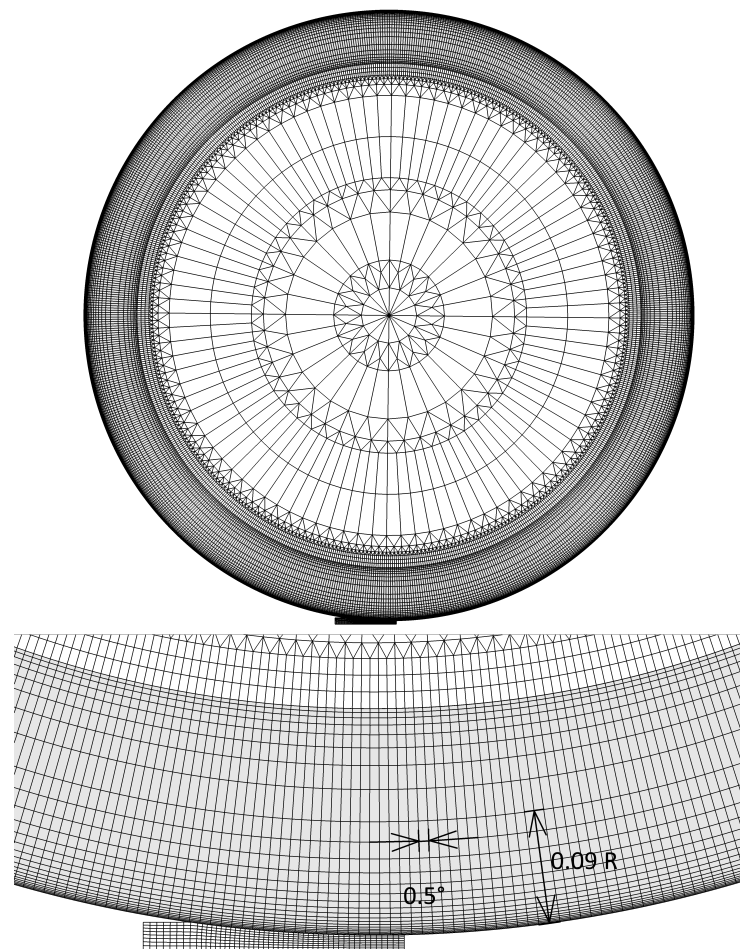

Figure 4. Global and local view of the mesh of the model (*R* is the external radius of the roll).

Table 5. Mesh elements used in the model.

	Type	Variables	Number
Roll	Linear quadrilateral	Temperature-displacement	19,968
Strip	Linear quadrilateral	Temperature-displacement	392
Shaft	Linear quadrilateral	Displacement	2528
	Linear triangular	Displacement	2336

2.4. Fatigue Modeling

To evaluate the thermo-mechanical fatigue damage, the equivalent strain criterion [34] was used. The equivalent strain ε_{eq} is assumed as the maximum Von Mises value during the cycle of the amplitude of the deviatoric strain tensor:

$$\varepsilon_{eq} = \max_t \sqrt{\frac{3}{2} \left(\boldsymbol{\varepsilon}'(t) - \boldsymbol{\varepsilon_m} \right) : \left(\boldsymbol{\varepsilon}'(t) - \boldsymbol{\varepsilon_m} \right)} \tag{4}$$

The deviatoric strain tensor is computed as follows:

$$\boldsymbol{\varepsilon}'(t) = \boldsymbol{\varepsilon}(t) - \frac{tr(\boldsymbol{\varepsilon}(t))}{3} \mathbf{I} \tag{5}$$

where $\mathbf{I}$ is the identity tensor. The mean strain tensor $\boldsymbol{\varepsilon_m}$ is the solution $\boldsymbol{\varepsilon_{dev}}$ of the following optimization problem:

$$\begin{cases} \min_{\boldsymbol{\varepsilon_{dev}}} \left\{ \max_t \sqrt{\frac{3}{2} \left(\boldsymbol{\varepsilon}'(t) - \boldsymbol{\varepsilon_{dev}} \right) : \left(\boldsymbol{\varepsilon}'(t) - \boldsymbol{\varepsilon_{dev}} \right)} \right\} \\ \\ tr(\boldsymbol{\varepsilon_{dev}}) = 0 \end{cases} \tag{6}$$

To compute the equivalent strain, the min–max optimization problem was solved [35] by using a Python optimization script, considering the Basin-hopping and Powell optimization methods.

3. Results

Table 6 summarizes the levels of the parameters investigated and the corresponding level index.

Table 6. Levels of the process parameters varied in the study.

Level	−2	−1	0	+1	+2
$h_{contact}$ $(\text{kW/m}^2\,^\circ\text{C})$	5	10	15	20	25
$T_{superheat}$ $(^\circ\text{C})$	20	30	40	50	60
h_{water} $(\text{kW/m}^2\,^\circ\text{C})$	1	5	10	15	20
u_{roll} (mm/s)	4	8	16	24	32

3.1. Temperature and Stress Fields

Figure 5a shows the temperature field after 8 cycles in the reference process conditions. The maximum temperature at the external surface of the roll reaches $T_{max} = 416\,^\circ\text{C}$ and minimum temperature $T_{min} = 80.1\,^\circ\text{C}$. There is a high temperature gradient at the external surface of the roll near the contact zone. This high temperature gradient is due to the high heat fluxes from the hot strip.

As shown in Figure 5b, the high temperature gradient causes high stresses near the contact area. High temperature and stress gradients are present at the external surface of the roll. Due to the high stresses, the yield condition is reached and the plastic flow is present during the first rotations of the roll.
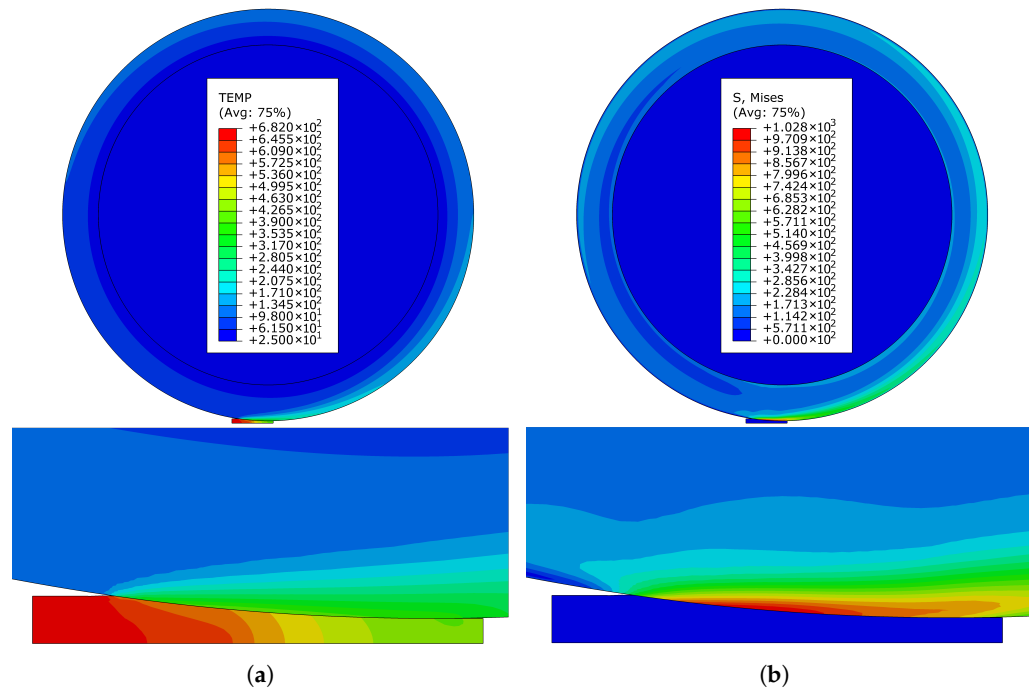
Figure 5. Global and strip–roll contact zone view: (**a**) temperature field T (°C), (**b**) Von Mises stress field σ_{VM} (MPa).

3.2. Stress Cycle

Figure 6 shows the stress history during the rotation of the roll, considering the radial σ_r, tangential σ_t, axial σ_z and shear σ_{rt} stresses. The angular position Angle = 0° in Figure 6 corresponds to the last angular position before the point comes in contact with the liquid metal as schematically represented in Figure 1. It is possible to distinguish two main parts during the rotation of the roll: contact zone (the left side of the plot) and free zone (the right side of the plot). Radial and shear stresses, σ_r and σ_{rt}, are principally determined by the mechanical contact interaction between the strip and the roll. Tangential and axial stresses, σ_t and σ_z, are mainly influenced by the temperature gradient and the interference fit interaction between the roll and the shaft.
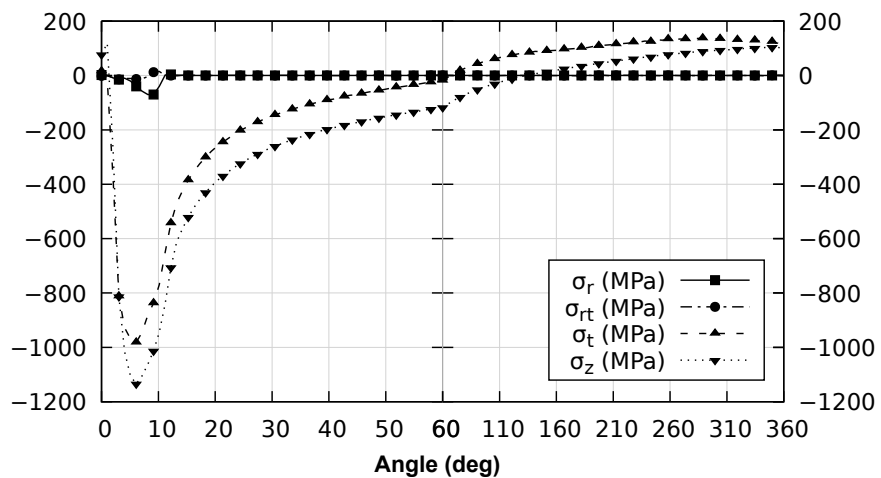

Figure 6. Radial σ_r, tangential σ_t, axial σ_z and shear σ_{rt} stresses during the rotation of the roll.

Figure 6 shows that high compressive stresses arise at the contact zone. At the contact zone, stresses, due to strip–roll mechanical contact interaction ($|\sigma_r|_{max} = 71.7$ MPa and

$|\sigma_{rt}|_{max} = 24.4\,\text{MPa}$), are lower than the those determined by the temperature gradient and the related thermal expansion ($|\sigma_t|_{max} = 981\,\text{MPa}$ and $|\sigma_z|_{max} = 1130\,\text{MPa}$). On the other hand, tensile stresses are present far away from the contact area: $\sigma_{t\,max} = 137\,\text{MPa}$ and $\sigma_{z\,max} = 104\,\text{MPa}$. These stresses are determined by the absence of the high temperature gradient at the surface, residual stresses and the global temperature field. The influence of the roll–shaft interference fit interaction is relatively negligible, with average roll–shaft contact pressure $p_{avg} = 0.58\,\text{MPa}$. The global temperature field and the thermal expansion of the roll decrease the effective interference and the contact pressure between the roll and the inner shaft.

The results show that a multiaxial out-of-phase cyclic load is present, which causes the thermo-mechanical fatigue (or the thermal-gradient fatigue) damage.

The stress cycle shows that the stress state is only roughly approximately bi-axial and in-phase with stresses directed along the external surface of the component (tangential and axial). The out-of-plane stress (radial direction) is caused by the mechanical contact, and its value is relatively small compared to the thermal stresses.

3.3. Influence of Process Parameters

3.3.1. Maximum Temperature of the Roll

Figure 7 shows the influence of the process parameters on the maximum temperature at the external surface of the roll T_{max}.
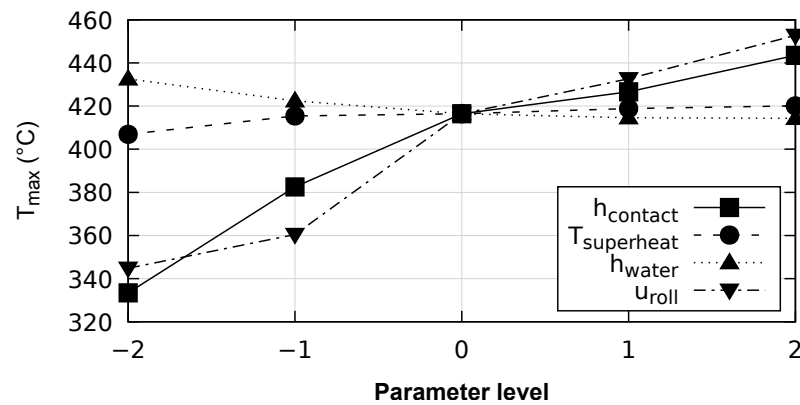

Figure 7. Maximum temperature on the external surface of the roll, depending on process parameters.

- As the strip–roll contact conductance coefficient rises from $h_{contact} = 5\,(\text{kW}/\text{m}^2\,°\text{C})$ to $h_{contact} = 25\,(\text{kW}/\text{m}^2\,°\text{C})$, the maximum temperature increases from $T_{max} = 333\,°\text{C}$ to $T_{max} = 444\,°\text{C}$. This effect is caused by the increasing heat fluxes between the strip and the roll at the contact zone;
- As the superheat temperature rises from $T_{superheat} = 20\,°\text{C}$ to $T_{superheat} = 60\,°\text{C}$, the maximum temperature rises from $T_{max} = 407\,°\text{C}$ to $T_{max} = 420\,°\text{C}$. This effect is caused by the higher heat fluxes from the liquid strip to the roll because of the higher strip inlet temperature;
- As the water-cooling heat transfer coefficient rises from $h_{water} = 1\,(\text{kW}/\text{m}^2\,°\text{C})$ to $h_{water} = 20\,(\text{kW}/\text{m}^2\,°\text{C})$, the maximum temperature decreases from $T_{max} = 433\,°\text{C}$ to $T_{max} = 414\,°\text{C}$. The cooling system tends to decrease the global temperature field of the roll;
- As the tangential velocity of the rolls rises from $u_{roll} = 4\,\frac{\text{mm}}{\text{s}}$ to $u_{roll} = 32\,\frac{\text{mm}}{\text{s}}$, the maximum temperature rises from $T_{max} = 345\,°\text{C}$ to $T_{max} = 453\,°\text{C}$. The maximum temperature of the roll T_{max} is mostly influenced by the level of the heat fluxes along the strip–roll contact length. In the considered process conditions for low roll speeds, the surface temperature of the strip decreases more rapidly and the rate of the temperature change of the roll is higher. In these conditions, the heat fluxes' effect on the point temperature along the strip–roll contact length tends to be lower. Thus, for

relatively low roll speeds, the material point tends to reach its maximum temperature earlier with lower values. The opposite behavior occurs for higher roll speeds. The roll speed also influences the average temperature of the component and, in particular, the minimum temperature at the outer surface during the roll rotation. As the roll speed increases, the average temperature tends to increase due to the lower cooling action of the water-cooling system during the roll cycle. It should be pointed out that this last phenomenon has little influence on the actual maximum temperature of the roll, which is more driven by the heat flux distribution along the contact zone.

Considering the levels taken into account, the tangential velocity of the rolls u_{roll} and the strip–roll contact conductance coefficient $h_{contact}$ are the most influential parameters in the evaluated range.

3.3.2. Maximum Contact Pressure

The influence between the maximum contact pressure $|\sigma_r|_{max}$ and the process parameters is shown in Figure 8.
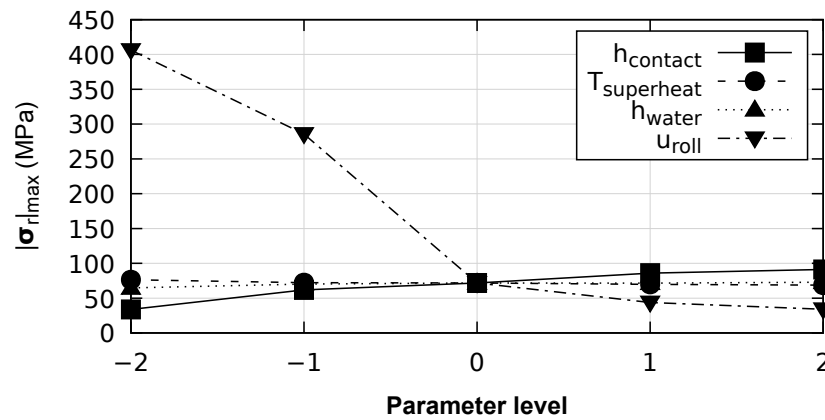

Figure 8. Maximum contact pressure on the external surface of the roll, depending on process parameters.

- As the strip–roll contact conductance coefficient rises from $h_{contact} = 5 \, (\text{kW/m}^2 \, {}^\circ\text{C})$ to $h_{contact} = 25 \, (\text{kW/m}^2 \, {}^\circ\text{C})$, the maximum contact pressure increases from $|\sigma_r|_{max} = 33.9 \, \text{MPa}$ to $|\sigma_r|_{max} = 91.3 \, \text{MPa}$;
- As the superheat temperature rises from $T_{superheat} = 20 \, {}^\circ\text{C}$ to $T_{superheat} = 60 \, {}^\circ\text{C}$, the maximum contact pressure decreases from $|\sigma_r|_{max} = 76.3 \, \text{MPa}$ to $|\sigma_r|_{max} = 68.8 \, \text{MPa}$;
- As the water-cooling heat transfer coefficient rises from $h_{water} = 1 \, (\text{kW/m}^2 \, {}^\circ\text{C})$ to $h_{water} = 20 \, (\text{kW/m}^2 \, {}^\circ\text{C})$, the maximum contact pressure increases from $|\sigma_r|_{max} = 64.6 \, \text{MPa}$ to $|\sigma_r|_{max} = 72.9 \, \text{MPa}$;
- As the tangential velocity of the rolls rises from $u_{roll} = 4 \, \frac{\text{mm}}{\text{s}}$ to $u_{roll} = 32 \, \frac{\text{mm}}{\text{s}}$, the maximum contact pressure decreases from $|\sigma_r|_{max} = 406 \, \text{MPa}$ to $|\sigma_r|_{max} = 34.0 \, \text{MPa}$. The influence of the velocity of the rolls is more relevant for smaller velocities. Due to more rapid solidification process at relatively low speed values, the mechanical contact pressure increases significantly and can contribute to the wear damage of the roll.

The mechanical contact interaction between the strip and the roll is mainly influenced by the solidification process of the strip along the casting direction. In particular, the mechanical contact stresses are influenced by the distance between the inlet surface and the point of the full solidification of the strip. This quantity is defined as sump depth and determines the main portion of the strip subjected to the rolling. As the solid portion of the strip undergoing the rolling increases (lower superheat temperature, lower roll speed, more efficient water-cooling system or more intense thermal contact), the contact pressure tends to increase. Considering the levels taken into account, the tangential velocity u_{roll} is the

most influential parameter. The influence of the strip–roll contact conductance coefficient $h_{contact}$ on the mechanical contact interaction is not negligible.

3.3.3. Accumulated Plastic Strain

Figure 9 shows the influence of the process parameters on the accumulated plastic strain after eight cycles of the roll.

It should be noted that, for all the simulations, the equivalent plastic strain increment tends to decrease during the eight cycles. In some cases, for example, for high values of the contact heat transfer coefficient, the plastic strain increment is visible only during the first two or even during the first load cycle only. Such a behavior was confirmed by running an additional 19 cycles of simulation for the reference conditions, which showed that, after the first cycles, the elastic shake-down phenomenon occurs. The attainment of the elastic shake-down conditions is even faster if the isotropic hardening of the material occurs.

In the reference conditions, the accumulated plastic strain after eight rotations of the roll $\varepsilon_{pl} = 1.79 \cdot 10^{-3}$. The accumulated plastic strain is related to the fatigue damage and, this is caused by the cyclic thermo-mechanical load followed by the plastic flow.
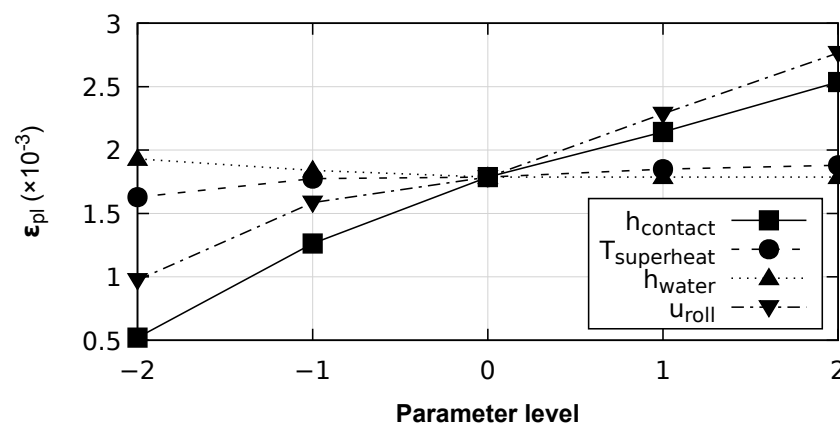

Figure 9. Accumulated equivalent plastic strain on the external surface of the roll, depending on process parameters.

- An increase in the strip–roll contact conductance coefficient from the value of $h_{contact} = 5 \, (\text{kW/m}^2 \, ^\circ\text{C})$ to $h_{contact} = 25 \, (\text{kW/m}^2 \, ^\circ\text{C})$ causes a monotonous increase in the accumulated plastic strain from $\varepsilon_{pl} = 5.21 \cdot 10^{-4}$ to $\varepsilon_{pl} = 2.54 \cdot 10^{-3}$. This is caused by the increasing contact heat fluxes between the strip and roll, determined by the contact conductance coefficient. Higher temperature gradients and thermal strains cause the stress to rise and the subsequent plastic flow;
- The influence of the melt superheat temperature is relatively small. As the melt superheat temperature rises from $T_{superheat} = 20 \, ^\circ\text{C}$ to $T_{superheat} = 60 \, ^\circ\text{C}$, the accumulated plastic strain increases from $\varepsilon_{pl} = 1.63 \cdot 10^{-3}$ to $\varepsilon_{pl} = 1.88 \cdot 10^{-3}$. These results are due to the higher thermal shock that occurs when the liquid aluminum touches the external surface of the cooled roll;
- As the tangential velocity of the rolls rises from $u_{roll} = 4 \, \frac{\text{mm}}{\text{s}}$ to $u_{roll} = 32 \, \frac{\text{mm}}{\text{s}}$, the accumulated plastic strain increases from $\varepsilon_{pl} = 9.75 \cdot 10^{-4}$ to $\varepsilon_{pl} = 2.77 \cdot 10^{-3}$.

The results show that the strip–roll contact conductance coefficient $h_{contact}$ and the tangential velocity of the rolls from u_{roll} are the most influential parameters in the plastic flow phenomenon. These two parameters contribute to the higher temperature gradient at the roll surface and the thermal softening of the material, causing damaging plastic flow.

3.3.4. Equivalent Strain

Figure 10 shows the relationship between the thermo-mechanical fatigue load, represented by the equivalent strain ε_{eq}, and the process parameters. In the reference conditions,

the equivalent strain $\varepsilon_{eq} = 2.58 \cdot 10^{-3}$. The results show that the most relevant parameter to consider to evaluate the fatigue damage is the contact conductance coefficient $h_{contact}$.
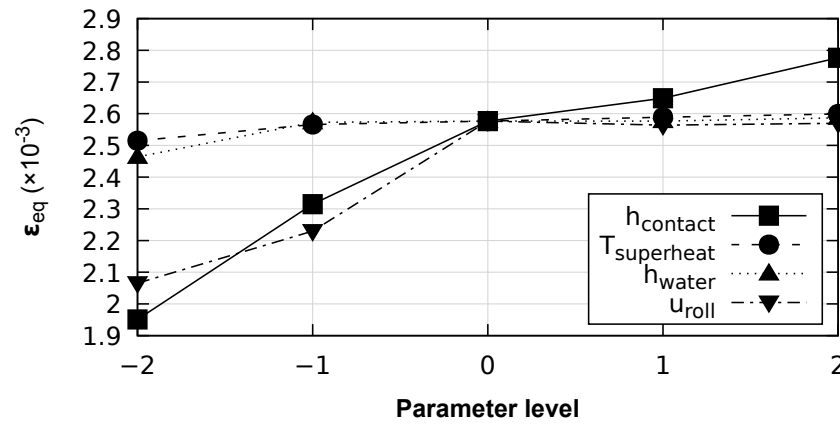

Figure 10. Equivalent strain value for the fatigue evaluation, depending on process parameters.

- In fact, as the strip–roll contact conductance coefficient rises from $h_{contact} = 5 \left(\mathrm{kW/m^2\,°C}\right)$ to $h_{contact} = 25 \left(\mathrm{kW/m^2\,°C}\right)$ the equivalent strain increases monotonously from $\varepsilon_{eq} = 1.95 \cdot 10^{-3}$ to $\varepsilon_{eq} = 2.78 \cdot 10^{-3}$. This result shows the importance of the contact heat fluxes between the strip and the roll in the thermo-mechanical fatigue damage. Due to a higher contact conductance, contact heat fluxes increase and so does the temperature gradient at the external surface of the roll;
- As the melt superheat temperature rises from $T_{superheat} = 20\,°C$ to $T_{superheat} = 60\,°C$, the equivalent strain slightly increases from $\varepsilon_{eq} = 2.51 \cdot 10^{-3}$ to $\varepsilon_{eq} = 2.60 \cdot 10^{-3}$;
- As the water-cooling heat transfer coefficient varies between $h_{water} = 1 \left(\mathrm{kW/m^2\,°C}\right)$ and $h_{water} = 20 \left(\mathrm{kW/m^2\,°C}\right)$, the equivalent strain remains almost constant, with a variation from $\varepsilon_{eq} = 2.46 \cdot 10^{-3}$ to $\varepsilon_{eq} = 2.59 \cdot 10^{-3}$;
- The influence of the tangential velocity of the rolls u_{roll} on the equivalent strain ε_{eq} is more relevant for small values of the roll speed. As the tangential velocity of the rolls rises from $u_{roll} = 4\,\frac{\mathrm{mm}}{\mathrm{s}}$ to $u_{roll} = 16\,\frac{\mathrm{mm}}{\mathrm{s}}$, the equivalent strain increases from $\varepsilon_{eq} = 2.07 \cdot 10^{-3}$ to $\varepsilon_{eq} = 2.58 \cdot 10^{-3}$. For higher values of the velocity, the equivalent strain remains almost constant. This behavior could suggest the influence of the contact pressure on the equivalent strain value for small velocities of the rolls. In fact, the contact pressure increases significantly for very low roll speeds, as shown in Figure 8, and influences the stress tensor state.

4. Conclusions

A two-dimensional coupled thermo-mechanical numerical model was defined. An explicit integration method and mixed Lagrangian-Eulerian analysis was performed, simulating eight rotations of the roll. The temperature-dependent properties were used and the latent heat of the aluminum was taken into account. The plastic behavior of the material of the roll was considered, and the kinematic cycling hardening model was defined based on the tensile test experimental data. The liquid aluminum initial temperature and the strip roll thermo-mechanical contact were defined with a contact conductance coefficient and the Coulomb friction model. The interference fit between the roll and the shaft was considered as well.

The results showed that a cyclic out-of-phase thermo-mechanical fatigue phenomenon occurs. Thermal stresses are considerably higher than those caused by the roll–strip mechanical contact.

Table 7 summarizes the results obtained and represents how a process parameter influences a damage parameter in the considered range. The results showed that, in the considered range, the most influential parameters are the heat contact conductance

coefficient $h_{contact}$, which dominates the thermo-mechanical load, and the tangential velocity of the rolls u_{roll}, which influences the thermal field and mechanical contact interaction between the roll and the strip. In fact, the results showed that, at a relatively low production rate, the contact pressure increases ($|\sigma_r|_{max} = 406$ MPa) and can aggravate the wear damage of the roll.

Table 7. Influence of the process parameters on the thermo-mechanical fatigue damage: $++$ relatively strong positive correlation, $(+)$ very small positive correlation, 0 relatively negligible influence, $(-)$ very small negative correlation, $--$ relatively strong negative correlation.

	T_{max}	$|\sigma_r|_{max}$	ε_{pl}	ε_{eq}
$h_{contact}$	$++$	$(+)$	$++$	$++$
$T_{superheat}$	0	0	0	0
h_{water}	$(-)$	0	0	0
u_{roll}	$++$	$--$	$++$	$+$

The obtained data could be used to make choices to minimize the damaging conditions of the roll and to reduce the thermo-mechanical fatigue phenomenon. On the other hand, the results could suggest which variables are more critical to design an experimental evaluation of the roll stress conditions and the prediction of their lifespans.

Author Contributions: Conceptualization, R.S.; methodology, R.S.; software, R.S.; validation, R.S. and A.M.; formal analysis, R.S.; investigation, R.S.; data curation, R.S.; visualization, R.S., N.Z. and A.M.; writing—original draft preparation, R.S.; writing—review and editing, R.S., N.Z. and A.M.; supervision, A.M.; project administration, A.M. All authors have read and agreed to the published version of the manuscript.

References

1. Bessemer, H. Improvement in the Manufacture of Iron and Steel. U.S. Patent N. 49053, 25 July 1865.
2. Maleki, A.; Taherizadeh, A.; Hoseini, N. Twin Roll Casting of Steels: An Overview. *ISIJ Int.* **2017**, *57*, 1–14. [CrossRef]
3. Akiyoshi, R.; Hori, M.; Matsui, K.; Hirata, A.; Fujita, K.; Ogawa, S. Roll Cooling Structure for Twin Roll Continuous Caster. U.S. Patent N. 5887644, 30 March 1999.
4. Zapuskalov, N. Twin Roll Comparison of Continuous Strip Casting with Conventional Technology. *ISIJ Int.* **2003**, *43*, 1115–1127. [CrossRef]
5. Ding, P.; Pan, F.; Jiang, B.; Wang, J.; Li, H.; Wu, J.; Xu, Y.; Wen, Y. Twin-roll strip casting of magnesium alloys in China. *Trans. Nonferrous Met. Soc. China* **2008**, *18*, 1003–6326. [CrossRef]
6. Haga, T.; Ikawa, M.; Watari, H.; Kumai, S. High speed twin roll casting of 6016 strip. *J. Achiev. Mater. Manuf. Eng.* **2006**, *18*, 371–374.
7. Zhao, H.; Li, P.; He, L. Microstructure and mechanical properties of an asymmetric twin-roll cast AZ31 magnesium alloy strip. *J. Mater. Process. Technol.* **2012**, *212*, 1670–1675. [CrossRef]
8. Sakaguchi, H.; Haga, T.; Watari, H.; Kumai, S. High speed twin roll casting of 6016 aluminium alloy strip. *J. Achiev. Mater. Manuf. Eng.* **2007**, *20*, 495–498.
9. Haga, T.; Suzuki, S. A high speed twin roll caster for aluminum alloy strip. *J. Mater. Process. Technol.* **2001**, *113*, 291–295. [CrossRef]
10. Gras, C.; Meredith, M.; Hunt, J.D. Microdefects formation during the twin-roll casting of Al–Mg–Mn aluminium alloys. *J. Mater. Process. Technol.* **2005**, *167*, 62–72. [CrossRef]
11. Chen, S.; Chen, J.; Yu, J.; Lv, L. Simulation of Microstructures in Solidification of Aluminum Twin-roll Casting. *J. Manuf. Process.* **2012**, *22*, 1452–1456. [CrossRef]
12. Hadadzadeh, A.; Wells, M.A. Inverse and centreline segregation formation in twin roll cast AZ31 magnesium alloy. *Mater. Sci. Technol.* **2015**, *31*, 1715–1726. [CrossRef]

13. Neuser, M.; Schaper, M.; Grydin, O. Mechanical and Microstructure Characterisation of the Hypoeutectic Cast Aluminium Alloy AlSi10Mg Manufactured by the Twin-Roll Casting Process. *J. Manuf. Mater. Process.* **2023**, *7*, 132. [CrossRef]
14. Guthrie, R.; Tavares, R. Mathematical and physical modelling of steel flow and solidification in twin-roll/horizontal belt thin-strip casting machines. *Mater. Sci. Technol.* **1998**, *22*, 851–872. [CrossRef]
15. Wang, D.; Zhou, C. A top side-pouring twin-roll caster for metals strips. *J. Mater. Process. Technol.* **2014**, *214*, 916–924. [CrossRef]
16. Lee, Y.S.; Kim, H.W.; Cho, J.H. Process parameters and roll separation force in horizontal twin roll casting of aluminum alloys. *J. Mater. Process. Technol.* **2015**, *218*, 48–56. [CrossRef]
17. Kim, M.-S.; Kim, H.-W.; Kim, S.-H.; Kumai, S. Role of Roll Separating Force in High-Speed Twin-Roll Casting of Aluminum Alloys. *Metals* **2019**, *9*, 645. [CrossRef]
18. Zeng, J.; Koitzsch, R.; Pfeifer, H.; Friedrich, B. Numerical simulation of the twin-roll casting process of magnesium alloy strip. *J. Mater. Process. Technol.* **2009**, *209*, 2321–2328. [CrossRef]
19. Saxena, A.; Sahai, Y. Modeling of Fluid Flow and Heat Transfer in Twin-Roll Casting of Aluminum Alloys. *Mater. Trans.* **2002**, *43*, 206–213. [CrossRef]
20. Hadadzadeh, A.; Wells, M.A. Mathematical modeling of thermo-mechanical behavior of strip during twin roll casting of an AZ31 magnesium alloy. *J. Magnes. Alloy* **2013**, *43*, 101–114. [CrossRef]
21. Lee, Y.S.; Kim, H.W.; Cho, J.H. Effect of Casting Parameters on Roll Separation Force during Twin Roll Casting. *Procedia Eng.* **2014**, *81*, 1547–1552. [CrossRef]
22. Toyoshima, S.; Takahashi, Y. A Numerical Simulation of Forming Processes for Semi-solid Materials. *ISIJ Int.* **1991**, *31*, 577–582. [CrossRef]
23. Lee, Y.S.; Kim, H.W.; Cho, J.; Chun, S.H. Coupled thermal-fluid-mechanics analysis of twin roll casting of A7075 aluminum alloy. *Met. Mater. Int.* **2017**, *23*, 923–929. [CrossRef]
24. Rodrigues, C.M.G.; Ludwig, A.; Wu, M.; Kharicha, A.; Vakhrushev, A. Two-phase viscoplastic model for the simulation of twin roll casting. *J. Mater. Process. Technol.* **2020**, *286*, 116814. [CrossRef]
25. Zapuskalov, N.; Vereschagin, M. Wear of Roll Surface in Twin-roll Casting of 4.5% Si Steel Strip. *ISIJ Int.* **2000**, *40*, 589–596. [CrossRef]
26. Saxena, A.; Sahai, Y. Modeling of Thermo-Mechanical Stresses in Twin-Roll Casting of Aluminum Alloys. *Mater. Trans.* **2002**, *43*, 214–221. [CrossRef]
27. Dündar, M.; Beyhan, B.; Birbaşar, O.; Altuner, H.M.; Işıksaçan, C. Surface Crack Characterization of Twin Roll Caster Shells and Its Influence on As-Cast Strip Surface Quality. In *Light Metals 2013*; Sadler, B.A., Ed.; The Minerals, Metals & Materials Series; Springer: Cham, Switzerland, 2013.
28. Wang, M.; Gu, T.; Yang, N.; Ma, Q. Study on microstructure and fatigue crack propagation of roll sleeves in an aluminum strip casting machine. *Eng. Fail. Anal.* **2013**, *31*, 338–343. [CrossRef]
29. ©Dassault Systèmes. *Abaqus/CAE. User's Guide*; Dassault Systèmes Simulia Corp.: Providence, RI, USA, 2014.
30. De Souza Neto, E.A.; Perić, D.; Owen, D.R.J. *Computational Methods for Plasticity: Theory and Applications*; John Wiley & Sons, Ltd.: Chichester, UK, 2008; p. 188.
31. Kenneth, C.M. *Recommended Values of Thermophysical Properties for Selected Commercial Alloys*; Woodhead Publishing Limited: Cambridge, UK, 2002; pp. 64–67.
32. Bondarenko, S.; Stolbchenko, M.; Schaper, M.; Grydin, O. Numerical Analysis of Twin-Roll Casting of Strips with Profiled Cross-Section. *Mater. Res.-Ibero-Am. J.* **2018**, *21*, e20171098. [CrossRef]
33. Li, B.Q. Producing thin strips by twin-roll casting—part II: Process modeling and development. *JOM* **1995**, *47*, 13–17.
34. Ciavarella, M.; Monno, F. A comparison of multiaxial fatigue criteria as applied to rolling contact fatigue. *Tribol. Int.* **2010**, *43*, 2139–2144. [CrossRef]
35. Bernasconi, A. Efficient algorithms for calculation of shear stress amplitude and amplitude of the second invariant of the stress deviator in fatigue criteria applications. *Int. J. Fatigue* **2002**, *24*, 649–657. [CrossRef]